2012

Effect of fiber orientation on shape and stability of air-water interface on submerged superhydrophobic electrospun thin coatings

B. Emami
Virginia Commonwealth University

H. Vahedi Tafreshi
Virginia Commonwealth University, htafreshi@vcu.edu

M. Gad-el-Hak
Virginia Commonwealth University, gadelhak@vcu.edu

G. C. Tepper
Virginia Commonwealth University, gctepper@vcu.edu

Emami, B., Tafreshi, H. V., & Gad-el-Hak, M., et al. Effect of fiber orientation on shape and stability of air-water interface on submerged superhydrophobic electrospun thin coatings. Journal of Applied Physics, 111, 064325 (2012).

Effect of fiber orientation on shape and stability of air–water interface on submerged superhydrophobic electrospun thin coatings

B. Emami, H. Vahedi Tafreshi,[a] M. Gad-el-Hak, and G. C. Tepper
Department of Mechanical and Nuclear Engineering, Virginia Commonwealth University, Richmond, Virginia 23284–3015, USA

(Received 14 December 2011; accepted 22 February 2012; published online 30 March 2012)

To better understand the role of fiber orientation on the stability of superhydrophobic electrospun coatings under hydrostatic pressures, an integro-differential equation is developed from the balance of forces across the air–water interface between the fibers. This equation is solved numerically for a series of superhydrophobic electrospun coatings comprised of random and orthogonal fiber orientations to obtain the exact 3D shape of the air–water interface as a function of hydrostatic pressure. More important, this information is used to predict the pressure at which the coatings start to transition from the Cassie state to the Wenzel state, i.e., the so-called critical transition pressure. Our results indicate that coatings composed of orthogonal fibers can withstand higher elevated hydrostatic pressures than those made up of randomly orientated fibers. Our results also prove that thin superhydrophobic coatings can better resist the elevated pressures. The modeling methodology presented here can be used to design nanofibrous superhydrophobic coatings for underwater applications. © *2012 American Institute of Physics*. [http://dx.doi.org/10.1063/1.3697895]

I INTRODUCTION

It is known that a hydrophobic surface with micro- or nano-scale roughness can produce superhydrophobicity.[1] When a superhydrophobic surface is brought in contact with water (the non-wetting fluid here), the surface pores can stay dry, entrapping air within their structure, which leads to a reduction in the solid surface area in contact with the water. A reduced contact area can result in a reduction in the skin-friction drag exerted on submerged objects such as ships or torpedoes in relative motion to the water. When the pore space on a superhydrophobic surface is filled with air, the system is at the Cassie state.[2] When water penetrates into the pores and completely replaces the air, the system transitions to the Wenzel state,[3] and the superhydrophobicity together with any drag-reducing advantage vanish. The hydrostatic pressure at which a superhydrophobic surface starts departing from the Cassie state, and therefore the superhydrophobic property starts to vanish, is herein referred to as the critical pressure.[4–6] Note that the focus of this study is the critical pressure of static or quasi-static penetration. Under dynamic penetration regimes, e.g., droplet impact on a superhydrophobic surface, the transition from Cassie state may occur at a much lower pressure.[7–9]

Balance of forces has been used to investigate the shape and stability of the air–water interface on superhydrophobic surfaces with ordered microstructures.[4,6,10–16] Our group has recently used balance of forces to calculate the shape and stability of the air–water interface on superhydrophobic surfaces with randomly distributed posts of dissimilar sizes, heights, and materials[17] as well as elliptical and polygonal shallow pores.[18]

In the current paper, we present a general method that can be used to obtain the exact 3D shape of the air–water interface on any arbitrary surface under elevated pressures. This information, specifically, can be used to obtain the critical pressure for surfaces and coating used in underwater applications.[19–25] We apply the balance of forces (and the first law of thermodynamics) on the air–water interface while accounting for the changes in the pressure of the entrapped air caused by the deflection of the interface. Our force balance analysis results in an integro-differential equation for the interface shape, which can then be solved numerically and used to obtain the pressure at which the surface departs from the Cassie state, i.e., the critical pressure. Unlike many previous works, the air–water meniscus is not forced to maintain a constant curvature inside pores of non-circular cross-sections.

Manmade superhydrophobic surfaces are often manufactured via microfabrication of hydrophobic grooves or posts. Microfabrication, however, is a costly process and cannot easily be applied to large surfaces with arbitrary shapes. An alternative approach to produce a superhydrophobic surface is by depositing hydrophobic fibers on a substrate using electrospinning.[26–29] With the traditional dc-electrospinning, however, one has less control over the coating microstructure (see Fig. 1(a)). Tepper and his co-workers have proposed the so-called dc-biased ac-electrospinning to better control the orientation of the fibers in a fibrous mat (see Refs. 7–9, 30, and 31 for detailed information about dc- and ac-electrospinning). The image shown in Fig. 1(b) is an example of a coating produced via dc-biased ac-electrospinning. It is expected that either dc- or ac-electrospinning can be used in the future to "engineer" superhydrophobic surfaces for different technologies including underwater/submerged applications.

The first attempt to predict the stability of air–water interface on an electrospun coating was the work of Tuteja *et al.*[16] These authors considered a simplified geometry of

[a]Author to whom correspondence should be addressed. Electronic mail: htafreshi@vcu.edu.

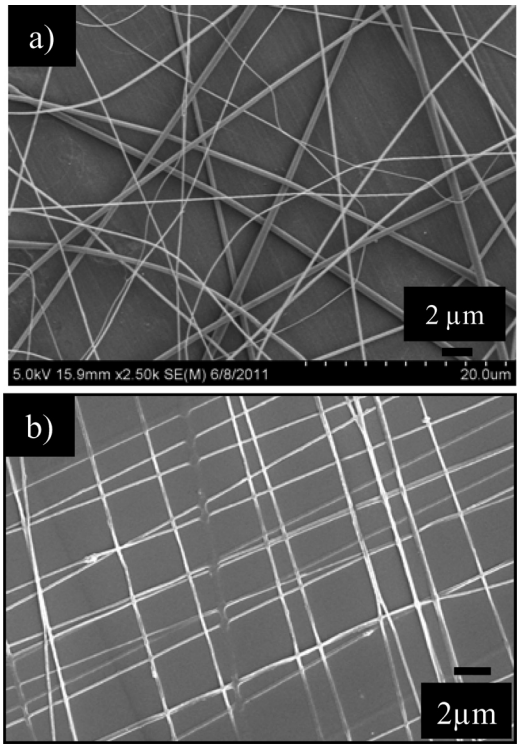

FIG. 1. Examples of microfabricated superhydrophobic coating. (a) fibrous superhydrophobic coating composed of randomly oriented fibers produced via dc-electrospinning; (b) fibrous superhydrophobic coating composed of orthogonally deposited fibers produced via dc-biased ac-electrospinning.

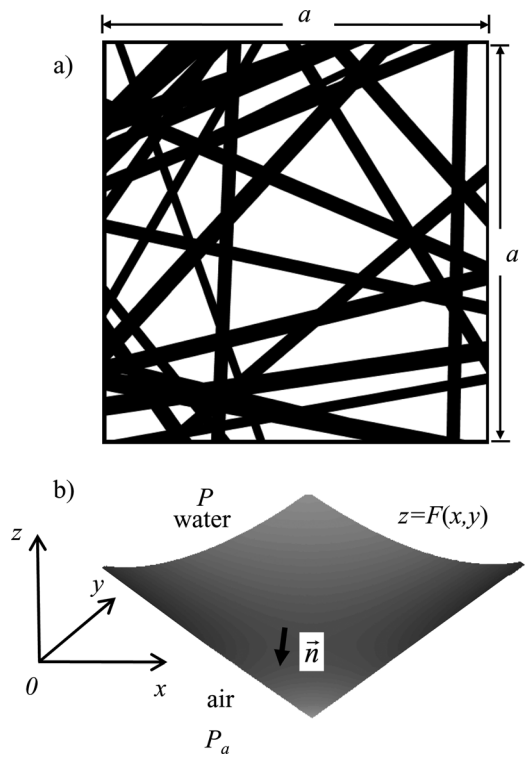

FIG. 2. (a) Top-view schematic of a fibrous superhydrophobic surface that consists of fibers of arbitrary widths and orientations. Note that the dark color represents fibers. (b) A force balance diagram corresponding to the air–water interface of a pore on the fibrous surface.

equally-spaced parallel fibers placed on a flat surface to develop two criteria for the evaluating the stability of the air–water interface under pressure. The calculation technique proposed in the present study not only predicts the stability of the air–water interface on more realistic fibrous geometries, i.e., surfaces made up of random deposition of fibers having random orientations, but also predicts the exact shape of the interface. Such information is particularly important for designing superhydrophobic nanofibrous coatings for underwater applications where resistance against elevated hydrostatic pressure is crucially important.

II PROBLEM FORMULATION

Predicting the shape of the air–water interface over a superhydrophobic 3D surface composed of fibers with random orientations and locations is prohibitively challenging. To simplify the problem, we assume the fibers behave as sharp edges, and therefore the air–water interface is pinned to the fibers. The underlying reason behind this assumption is that, unlike large round fibers, a thin nanofiber can be treated as a sharp edge to which an interface can be pinned.[32,33] Furthermore, we assume that due to the thinness of the nanofiber coatings (i.e., very few layers of fibers), the air–water interface touches all the fibers (i.e., negligible height difference between the fibers). The latter assumption allows us to consider 2D domains for studying the actual 3D nanofibrous coatings.

As can be seen from Figs. 1 and 2(a), the pores between fibers form arbitrary polygonal pores with shallow depths. The fibrous network shown in Fig. 2(a) is developed via the μ-randomness algorithm,[34] and has also fully described in our previous studies with virtual 3D fibrous media.[35,36]

Figure 2(b) shows a simple sketch representing the air–water meniscus between fibers. By applying balance of forces on the meniscus $z = F(x, y)$ one gets,

$$P + P_\infty - P_a - \sigma \nabla . \vec{n} = 0, \tag{1}$$

where P is the gauge hydrostatic pressure, P_∞ is the ambient pressure, P_a is the pressure in the entrapped air, σ is the air–-water surface tension, and $\vec{n}$ is the surface unit normal vector. Let us define a function $G(x, y, z) \equiv F(x, y) - z$ (obviously, $G(x, y, z) = 0$ on the meniscus surface). It can be shown that the meniscus surface unit normal vector, $\vec{n}$, can be calculated as a function of G, thus,

$$\vec{n} = \nabla G / |\nabla G| \tag{2}$$

Hence,

$$\begin{aligned} n_1 &= \left(1 + F_x^2 + F_y^2\right)^{-1/2} F_x \\ n_2 &= \left(1 + F_x^2 + F_y^2\right)^{-1/2} F_y \\ n_3 &= -\left(1 + F_x^2 + F_y^2\right)^{-1/2} \end{aligned} \tag{3}$$

where n_1, n_2, and n_3 are the components of $\vec{n}$ in x, y, and z directions, respectively, and $F_x = \partial F / \partial x$, and $F_y = \partial F / \partial y$. According to the force balance, the interface forms a different shape as the hydrostatic pressure P varies. This changes the volume and, therefore, the pressure of the air entrapped in the

pore, P_a. Here, we assume that dissolution of the entrapped air into water is insignificant, and therefore the air does not escape from the pores when the surface is in Cassie state. Because the entrapped air is in thermal equilibrium with water, one can assume an isothermal equilibrium. The ideal gas law thus yields $P_a = P_\infty V_{a,0}/V_a$, where $V_{a,0}$ is the total porous volume of the fibrous coating (volume of the entrapped air at $P=0$), and V_a is the entrapped air volume. Note that $V_{a,0}$ can be calculated based on the thickness, surface area, and solid volume fraction of the fibrous coating. It can be shown that,

$$V_a = V_{a,0} + \int_\Omega F(x,y)dx\,dy \tag{4}$$

where Ω represents the computational domain, i.e., the pore surface between fibers. Equation (1) then reduces to,

$$\sigma\left(1+F_y^2\right)F_{xx} + \sigma\left(1+F_x^2\right)F_{yy} - 2\sigma F_x F_y F_{xy} - \left[P + P_\infty\left(1 - \frac{V_{a,0}}{V_{a,0} + \int_\Omega F(x,y)dx\,dy}\right)\right]\left(1+F_x^2+F_y^2\right)^{3/2} = 0, \tag{5}$$

where the indices x and y represent $\partial/\partial x$ and $\partial/\partial y$, respectively.

The above integro-differential equation can be solved numerically to obtain the shape of the interface under different hydrostatic pressures. As per the boundary conditions, F vanishes on the walls,

$$F|_{\partial\Omega} = 0 \tag{6}$$

and its normal derivatives vanish on the domain boundaries due to symmetry,

$$\frac{\partial F}{\partial n}|_{\partial C} = 0 \tag{7}$$

where $\partial\Omega$ represents the fiber walls, and ∂C represents the domain boundaries.

Using the computed air–water interface surface, $z = F(x,y)$, one can calculate the critical hydrostatic pressure at which departure from the Cassie state starts. The failure occurs when the angle between the meniscus and the solid wall, i.e., the fibers, reaches the air–water–solid flat surface contact angle θ.[22–25,27] Hence, the superhydrophobicity is dependent on the slope of the meniscus at the fibers. Therefore, unless the condition,

$$|\nabla F|_{\partial\Omega} < |\cot\theta| \tag{8}$$

holds, the surface departs from the Cassie state.

We assume that the superhydrophobic surface fails, if the above condition does not hold at any point on the surface. This is because, given the layered nature of electrospun coatings, it is easier for a non-wetting fluid to penetrate into a fibrous structure in the in-plane direction as opposed to the through-plane direction. The above argument is deduced from the established fact that permeability of fibrous structures is higher in the in-plane direction when the structure is layered (see Ref. 36 for more information).

We used the finite element FLEXPDE program from PDE Solutions Inc. to solve Eqs. (5)–(7). All of the numerical solutions were run on a workstation with a dual core 2.4 GHz CPU, and 4 GB of RAM; each solution took only a few minutes. Careful attention was paid to ensure that the results of our calculations are not dependent on the choice of the mesh size.

A. A Thermodynamics Viewpoint

It is worth mentioning that Eq. (5) can also be derived by applying the first law of thermodynamics on the air–water interface. Let us assume that the interface is in equilibrium at a hydrostatic pressure P, and forms a shape $z = F(x,y)$. If the hydrostatic pressure increases infinitesimally to $P+\delta P$, the interface shape changes infinitesimally to $F+\delta F$. The first law of thermodynamics requires that the work done on a system be equal to the change in the potential energy of that system. Therefore, the work done by the hydrostatic pressure, minus the work done to increase the enthalpy of the entrapped air, equals the change in the surface energy of the interface,

$$\int_\Omega (P_\infty + P + \delta P)|\delta F|dx\,dy - \int_\Omega (P_\alpha + \delta P_\alpha)|\delta F|dx\,dy = \delta\int_\Omega L\left(F_x,F_y\right)dx\,dy \tag{9}$$

where the Lagrangian $L\left(F_x,F_y\right) \equiv \sigma\left(1+F_x^2+F_y^2\right)^{-1/2}$, and the right-hand side of the above equation shows the change in the surface potential energy, which can be further simplified by calculus of variables,

$$\delta\int_\Omega L\left(F_x,F_y\right)dx\,dy = \int_\Omega\left(\frac{\partial L}{\partial F_x}\delta F_x + \frac{\partial L}{\partial F_y}\delta F_y\right)dx\,dy \tag{10}$$

Using integration by parts, one gets,

$$\delta\int_\alpha L\left(F_x,F_y\right)dx dy = \int_y\left[\left(\frac{\partial L}{\partial F_x}\delta F\right)_{\partial\Omega} - \int_x \frac{d}{dx}\left(\frac{\partial L}{\partial F_x}\right)\delta F dx\right]dy + \int_x\left[\left(\frac{\partial L}{\partial F_y}\delta F\right)_{\partial\Omega} - \int_y \frac{d}{dy}\left(\frac{\partial L}{\partial F_y}\right)\delta F dy\right]dx \tag{11}$$

Because we assume the interface is pinned to the fiber edges, F is fixed on the boundaries, and so $\delta F = 0$ on $\partial\Omega$. The above relation then reduces to,

$$\delta\int_\Omega L\left(F_x,F_y\right)dx\,dy = -\int_\Omega\left[\frac{d}{dx}\left(\frac{\partial L}{\partial F_x}\right) + \frac{d}{dy}\left(\frac{\partial L}{\partial F_y}\right)\right]\delta F dx\,dy \tag{12}$$

Substituting for the Lagrangian $L\left(F_x,F_y\right)$ into the right-hand side of Eq. (12), one gets,

$$\delta\int_\Omega L\left(F_x,F_y\right)dx\,dy = -\sigma\int_\Omega\left(1+F_x^2+F_y^2\right)^{-\frac{3}{2}} \times\left[\left(1+F_y^2\right)F_{xx} + \left(1+F_x^2\right)F_{yy} - 2F_xF_yF_{xy}\right]\delta F dx\,dy \tag{13}$$

Substituting the above relation into the right-hand side of Eq. (9), and considering the fact that $\delta F \leq 0$ (because the interface moves downward as the hydrostatic pressure increases), we get,

$$\int_{\Omega}\left\{-P-P_{\infty}+P_a+\sigma\left(1+F_x^2+F_y^2\right)^{-\frac{3}{2}} \left[\left(1+F_y^2\right)F_{xx}+\left(1+F_x^2\right)F_{yy}-2F_xF_yF_{xy}\right]\right\}\delta F\,dx\,dy=0 \tag{14}$$

where the second-order terms are eliminated in the above equation. Therefore,

$$\left(P+P_{\infty}-P_a\right)\left(1+F_x^2+F_y^2\right)^{3/2} =\sigma\left[\left(1+F_y^2\right)F_{xx}+\left(1+F_x^2\right)F_{yy}-2F_xF_yF_{xy}\right] \tag{15}$$

and Eq. (5) then follows.

The above analysis is equivalent to minimizing the total surface energy of and the work done on the interface, E,

$$E[F]=\int_{\Omega}\left[\left(P_{\infty}+P-P_a\right)|F|+\sigma\left(1+F_x^2+F_y^2\right)^{-1/2}\right]dx\,dy \tag{16}$$

where E is a functional of the interface shape F. The corresponding Euler-Lagrange equation[37] of the above integral results in Eq. (5).

III RESULTS AND DISCUSSION

To demonstrate the capabilities of our method, we calculated the meniscus shape and the critical pressure for a superhydrophobic surface with randomly oriented fibers of dissimilar random diameters ranging from 50 nm to 150 nm, corresponding to a gas area fraction, ϕ_g, of 70%. The flat surface contact angle, the thickness t, and the solid volume fraction of the fibrous coatings were arbitrarily chosen to be 120°, 450 nm, and 2.5%, respectively. Figures 3(a) and 3(b) present the predicted meniscus surfaces, at hydrostatic pressures of 5 kPa and 46 kPa, respectively. As expected, our results show that the deflection of the meniscus, and therefore its slope, increase with pressure. Figure 3(c) shows the contours of meniscus gradient at a hydrostatic pressure P of 46 kPa. As can be seen, the maximum meniscus gradient occurs inside the largest pore. This is expected, because the larger the pore size, the smaller the meniscus's radius of curvature at a given hydrostatic pressure, and hence the smaller the required capillary forces. At $P=46$ kPa, the maximum value of the meniscus gradient approaches 0.58 ($=|\cot\theta|=|\cot 120^{o}|$), and so the superhydrophobicity starts to diminish.

The formulations given in this paper can easily be used to quantitatively show that thicker coatings have less resistance against the elevated pressures, as the effects of entrapped air compression becomes less important when the volume of the entrapped air is much greater than that displaced due to deflection of the interface.

To compare the stability of thin dc- and ac-electrospun nanofiber coatings, we considered two fibrous surfaces with identical microstructural parameters (e.g., fiber diameter, porosity, thickness) but different fiber in-plane orientations. Figures 4(a) and 4(b) show an example of the calculations conducted for the dc- and ac-electrospun coatings, respectively. A fiber diameter d of 100 nm, and a range of gas area

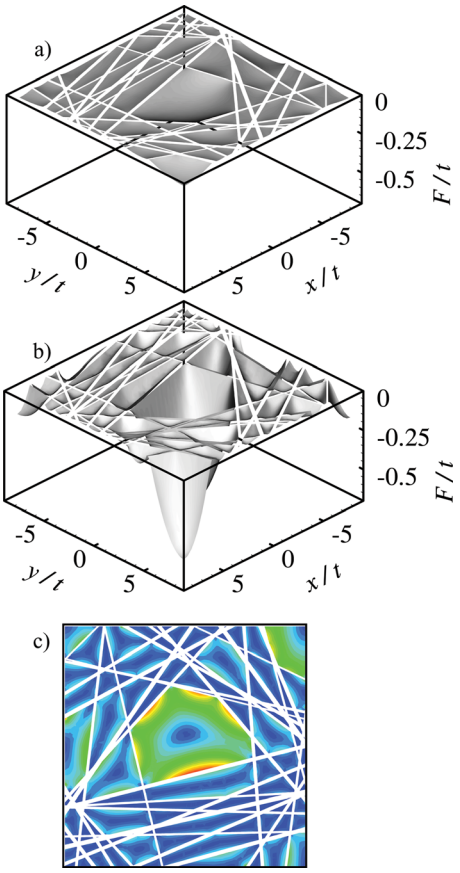

FIG. 3. Calculated meniscus surfaces for a fibrous superhydrophobic surface (a) at $P=5$ kPa; and (b) at the critical pressure $P=46$ kPa; (c) calculated gradient ($|\nabla F|$) contours at the critical pressure $P=46$ kPa. Blue to red represents 0 to 0.6 in the contours.

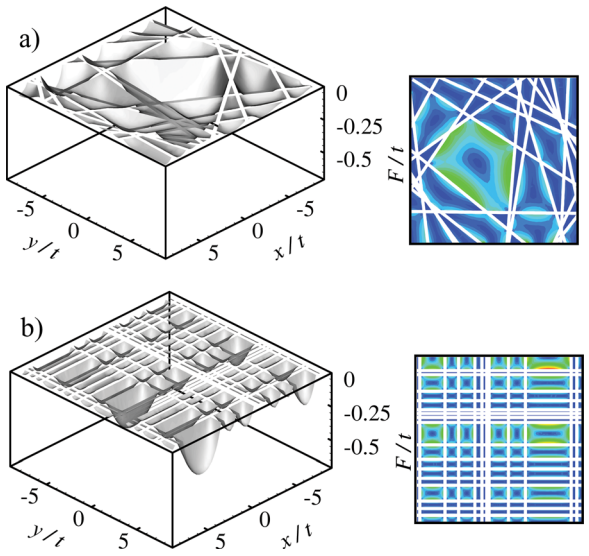

FIG. 4. Calculated meniscus surfaces and gradient contours at the critical pressure for (a) dc-electrospun, (b) ac-electrospun fibrous surface. Blue to red represents 0 to 0.6 in the contours.

fractions from 70% to 90% were arbitrarily considered for both surfaces. The contact angle, the coatings' thickness, and the coatings' solid volume fraction were also arbitrarily chosen to be 120°, 300 nm, and 2.5%, respectively. To ensure that our calculations are statistically representative, we conducted our calculations over an ensemble of at least five statistically identical fibrous structures in each case. Moreover, to ensure that our computational domain is large enough to statistically represent a given fibrous coating, we considered a given nanofibrous coating with randomly oriented fibers, and incrementally increased the size of our simulation domain to study effects of domain size on the critical pressure calculation. Figure 5 shows the ensemble-averaged predicted critical pressure P_{cr} versus the size of the computational domain a, normalized by the fiber diameter d. As can be seen, the results become independent of the domain size at $a = 40d$. A $50d \times 50d$ domain was then used for all of the calculations.

Figure 6 shows the critical pressure values computed at different gas area fractions for the dc-electrospun and ac-electrospun surfaces. As expected, the critical pressure reduces as the gas area fraction, and hence the average size of the pores, increases. Although these numerical values may not correspond to any particular coatings, as our input numbers were chosen arbitrarily, they clearly show that surfaces with orthogonal fibers can better resist the elevated hydrostatic pressures. This effect can be explained by considering the differences in the shape of pores on the coatings with orthogonal and randomly oriented fibers. Orthogonal fibers on an ac-electrospun surface form rectangular pores, while pores on a dc-electrospun surface correspond to arbitrary polygons because of the random orientation of fibers. Because the stability of a meniscus largely depends on the balance of capillary and hydrostatic pressures, one can expect the critical pressure to be proportional to the ratio of the pore perimeter to its cross-sectional area—the higher the ratio, the larger the critical hydrostatic pressure. For simplicity, let us assume that each pore cross-section has equal sides. The perimeter-to-area ratio for an equilateral polygon of n sides is $4\tan(\pi/n)/l$, where l is the length of each side. It can be shown that this ratio decreases as n increases. Pores of a surface with orthogonal fibers correspond to $n = 4$, whereas pores on a surface with randomly oriented fibers may correspond to higher values of n and therefore to lower critical pressures.

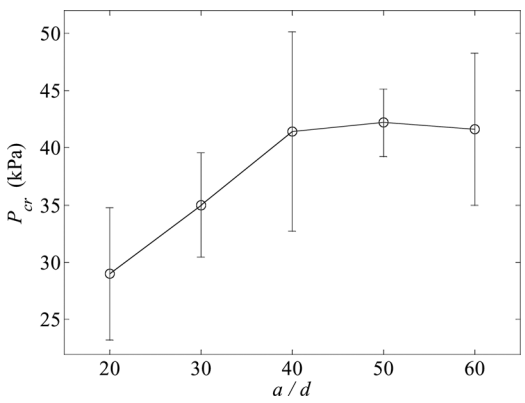

FIG. 5. Predicted critical pressure vs the size of the computational domain. Calculations become domain size independent, at a domain size of $40d \times 40d$, where d is the fiber diameter.

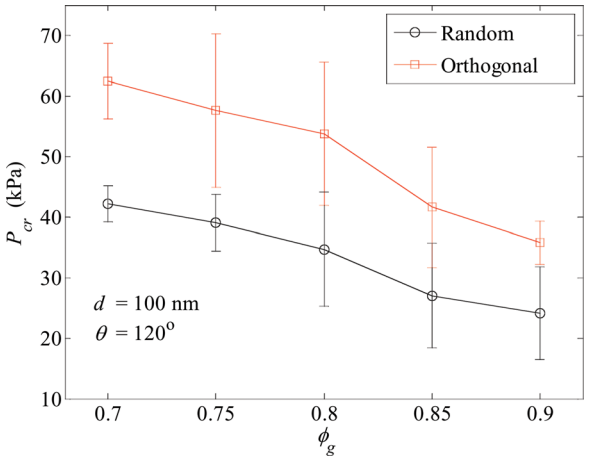

FIG. 6. Predicted critical pressure values vs gas area fraction, for the dc-electrospun and ac-electrospun coatings with $d = 100$ nm, and $\theta = 120°$.

We also used our methodology to study the effects of fiber diameter d and contact angle θ on critical pressure. In all of the cases, the coating thickness was chosen to be three times greater than the fiber diameter. Figure 7 shows the critical pressures computed at different fiber diameters, ranging from 100 nm to 500 nm, for the dc- and ac-electrospun surfaces with a gas area fraction ϕ_g of 70%, and a contact angle θ of 120°. A coating solid volume fraction of 2.5% was assumed for the calculations shown in Fig. 7. As can be seen, critical pressure increases as the fiber diameter decreases. This is because at a given gas area fraction, reducing the fiber diameter results in a more populous network of fibers leading to formation of smaller (but more in quantity) pores. As the failure depends on the size of the pores rather than their quantity, decreasing the fiber diameter results in an increase in critical pressure.

Figure 8 shows the critical pressure values obtained for different values of θ for both the dc- and ac-electrospun surfaces having a constant gas area fraction of 70%, and a fiber diameter of 100 nm. As expected, a smaller equilibrium contact angle results in a less hydrophobic surface, and of course, a lower critical pressure.

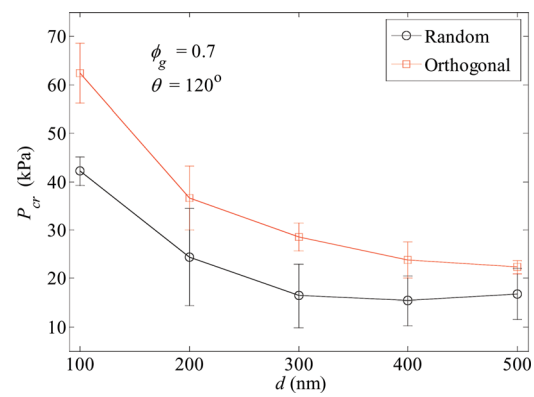

FIG. 7. Predicted critical pressure values vs fiber diameter, for the dc-electrospun and ac-electrospun coatings with $\phi_g = 0.7$, and $\theta = 120°$.

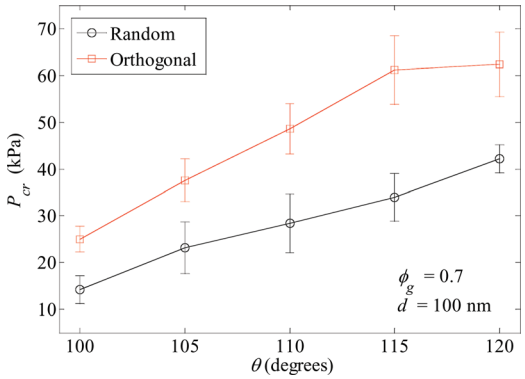

FIG. 8. Predicted critical pressure values vs contact angle, for the dc-electrospun and ac-electrospun coatings with $\phi_g = 0.7$, and $d = 100$ nm.

IV CONCLUSIONS

In this work a mathematical framework is developed to predict the critical hydrostatic pressure above which a nanofibrous superhydrophobic coating starts transitioning the Wenzel state. The resulting integro-differential equation can serve as a means for designing superhydrophobic coatings for underwater applications where elevated hydrostatic pressures. Our results indicate that a superhydrophobic surface with an orthogonal nanofibrous structure corresponds to a higher critical pressure compared with a similar surface comprised of randomly oriented nanofibers. Moreover, at a given gas area fraction, reducing the diameter of the fibers improves resistance of the surface against hydrostatic pressures.

ACKNOWLEDGMENTS

The authors would like to acknowledge the financial support for this work provided by Defense Advanced Research Projects Agency (DARPA) contract number W91CRB-10–1–0003. In addition, B.E. and H.V.T. also acknowledge the VCU Presidential Research Incentive Program (PRIP) for partial support.

[1]J. P. Rothstein, Annu. Rev. Fluid Mech. **42**, 89 (2010).
[2]A. B. D. Cassie and S. Baxter, Trans. Faraday Soc. **40**, 546 (1944).
[3]R. N. Wenzel, Ind. Eng. Chem. **28**, 988 (1936).
[4]B. Liu and F. F. Lange, J. Colloid Interf. Sci. **298**, 899 (2006).
[5]X. Sheng and J. Zhang, Colloid and Surf., A **377**, 374 (2011).
[6]B. Emami, T. Bucher, H. V. Tafreshi, M. Gad-el-Hak, and G. C. Tepper, Colloid and Surf., A **385**, 95 (2011).
[7]A. N. Lembach, H-B. Tan, I. V. Roisman,T. Gambaryan-Roisman, Y. Zhang, C. Tropea, and A. L. Yarin, Langmuir **26**, 9516 (2010).
[8]C. M. Weickgenannt, Y. Zhang, A. N. Lembach, H.-B. Tan, I. V. Roisman, T. Gambaryan-Roisman, A. L. Yarin, and C. Tropea, Phys. Rev. E **83**, 036305 (2011).
[9]C. M. Weickgenannt, Y. Zhang,S. Sinha-Ray, I. V. Roisman, T. Gambaryan-Roisman, C. Tropea, and A. L. Yarin, Phys. Rev. E **84**, 036310 (2011).
[10]C. W. Extrand, Langmuir **18**, 7991 (2002).
[11]C. W. Extrand, Langmuir **20**, 5013 (2004).
[12]Q. S. Zheng, Y. Yu, and Z. H. Zhao, Langmuir **21**, 12207 (2005).
[13]E. J. Lobaton and T. R. Salamon, J. Colloid Interf. Sci. **314**, 184 (2007).
[14]M. C. Salvadori, M. Cattani, M. R. S. Oliveira, F. S. Teixeira, and I. G. Brown, J. Appl. Phys. **108**, 024908 (2010).
[15]C. W. Extrand, Langmuir **27**, 6920 (2011).
[16]A. Tuteja, W. Choi, J. M. Mabry, G. H. McKinely, and R. E. Cohen, Proc. Natl. Acad. Sci. U.S.A. **105**, 18200 (2008).
[17]B. Emami, H. V. Tafreshi,M. Gad-el-Hak, and G. C. Tepper, Appl. Phys. Lett. **98**, 2031061 (2011).
[18]B. Emami, H. V. Tafreshi, M. Gad-el-Hak, and G. C. Tepper, Appl. Phys. Lett. **100**, 013104 (2012).
[19]A. Marmur, Langmuir **22**, 1400 (2006).
[20]M. Sakai, T. Yanagisawa, A. Nakajima, Y. Kameshima, and K. Okada, Langmuir **25**, 13 (2009).
[21]M. S. Bobji, S. V. Kumar, A. Asthana, and R. N. Govardhan, Langmuir **25**, 12120 (2009).
[22]R. Poetes, K. Holtzmann, K. Franze, and U. Steiner, Phys. Rev. Lett. **105**, 166104 (2010).
[23]G. Mchale, M. I. Newton, and N. J. Shirtcliff, Soft Matter **6**, 714 (2010).
[24]P. Forsberg, F. Nikolajeff, and M. Karlsson, Soft Matter **7**, 104 (2011).
[25]M. A. Samaha, F. O. Ochanda, H. V. Tafreshi, G. C. Tepper, and M. Gad-el-Hak, Rev. Sci. Instrum. **82**, 0451091 (2011).
[26]D. H. Reneker and A. L. Yarin, Polymer **49**, 2387 (2008).
[27]M. Ma, R. M. Hill, and G. C. Rutledge, J. Adhes. Sci. Technol. **22**, 1799 (2008).
[28]M. Ma, Y. Mao, M. Gupta, K. K. Gleason, and G. C. Rutledge, Macromolecules **38**, 9742 (2005).
[29]A. Singh, L. Steely, and H. R. Allcock, Langmuir **21**, 11604 (2005).
[30]S. Sarkar, S. C. Deevi, and G. Tepper, Macromol. Rapid Comm. **28**, 1034 (2007).
[31]O. Ochanda, M. A. Samaha, H. V. Tafreshi, G. C. Tepper, and M. Gad-el-Hak, J. Appl. Polym. Sci. **123**, 1112 (2011).
[32]P. Singh and D. D. Joseph, J. Fluid Mech. **530**, 31 (2005).
[33]D. Quere, Annu. Rev. Mater. Res. **38**, 71 (2008).
[34]B. Pourdeyhimi, R. Ramanathan, and R. Dent, Text. Res. J. **66**, 713 (1996).
[35]Q. Wang, B. Maze, H. V. Tafreshi, and B. Pourdeyhimi, Model. Simul. Mater. Sci. Eng. **15**, 855 (2007).
[36]M. A. Tahir and H. V. Tafreshi, Phys. Fluids **21**, 0836041 (2009).
[37]O. Buhler, *A Brief Introduction to Classical, Statistical, and Quantum Mechanics* (American Mathematical Society, 2000).